Journal of Materials Chemistry C

Accepted Manuscript

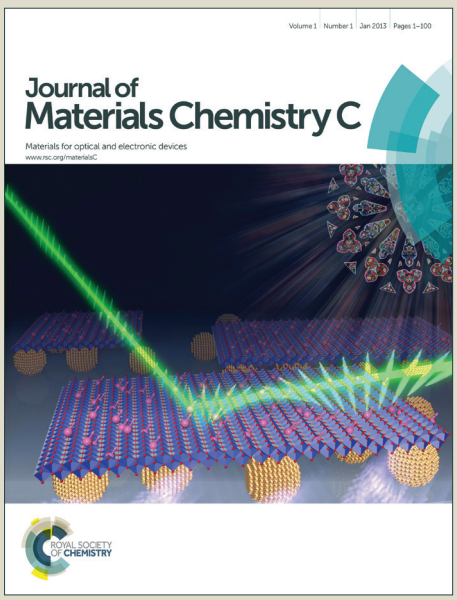

ROYAL SOCIETY OF CHEMISTRY

www.rsc.org/materialsC

Catalytically induce nanographite phase by platinum-ion implantation/annealing process to improve the field electron emission properties of ultrananocrystalline diamond films

Kamatchi Jothiramalingam Sankaran,[a] Kalpataru Panda,[b] Balakrishnan Sundaravel,[c] Nyan-Hwa Tai,[a] * and I-Nan Lin[d] *

We report the Pt-ion implantation/annealing process for enhancing the electrical conductivity and the field electron emission (FEE) properties of ultrananocrystalline diamond (UNCD) films. Platinum ion implantation is performed on UNCD films at room temperature with implantation energy of 500 keV and ion dosages are varied from 1 x 10^{15} to 1 x 10^{17} ions/cm^2 at an ion flux of 1.035 x 10^{12} ions/cm^2/s. The UNCD films, which were Pt-ion implanted with 1 x 10^{17} ions/cm^2 and annealed at 600°C possess high electrical conductivity of 94.0 (ohm-cm)$^{-1}$ and low turn-on field of 4.17 V/μm with high FEE current density of 5.08 mA/cm^2 (at 7.2 V/μm). The current imaging tunneling spectroscopy and local current-voltage curves of scanning tunneling spectroscopic measurements illustrated that the electrons are predominantly emitted from the grain boundaries. Transmission electron microscopy examinations reveal that the implanted Pt-ions first formed Pt nanoparticles in UNCD films and then catalytically induced the formation of nanographitic phase at the grain boundaries during the annealing process. Consequently, the formation of Pt nanoparticles, which induced abundant nanographitic phases in Pt-ion implanted/annealed UNCD films, are believed to be the genuine factors, resulting in high electrical conductivity and excellent FEE properties of the films.

Keywords: *ultrananocrystalline diamond films, platinum ion implantation, field electron emission, nanographitic phases*

1. Introduction

Ultrananocrystalline diamond (UNCD) film is a special form of diamond that has recently attracted the research community because of its improved field electron emission (FEE)

properties, along with its ultra-small grain size (2–5 nm) and very smooth surface characteristics.[1] The grains are diamond, having a sp^3 character, whereas the grain boundaries have a mixture of sp^2, sp^3, hydrocarbon, and amorphous carbon (*a-C*) with the sp^2 character being predominant.[2] Because of the low turn-on field and the large field emission current density of UNCD, as compared to other forms of diamond (microcrystalline or nanocrystalline), this material illustrates potential applications such as cold cathode emitters and other vacuum microelectronic devices. The promise that a diamond or an UNCD film stands as a material for the fabrication of cold cathode or other electron emitting devices necessitates the film to be conductive. Inducing graphitic grain boundary phases by incorporation of N_2 into plasma during UNCD film's growth can efficiently improve the electrical conductivity of 186 $(ohm\text{-}cm)^{-1}$ and enhance the FEE properties of the films.[3–6] However, a high growth temperature (about 800°C) is necessary to activate the dopants for creating high conductivity in the UNCD films.[5–8]

Ion implantation technique has long been utilized to modify the properties of diamond materials through controlled doping with the selection of dopants.[9–11] Recent reports showed that oxygen and phosphorous ion implantation induced *a-C* phases in the grain boundaries of UNCD films which provide *n*-type conductivity.[12,13] But the electrical conductivity of these UNCD films is not adequately high due to the presence of low conductivity *a-C* phases in the grain boundaries and, thus, confines the FEE properties of these films. The conversion of *a-C* phase into graphitic phase seems to be a probable approach. Hence a process, which can induce efficiently the formation of graphitic phases in the grain boundaries of UNCD films to accomplish high conductivity, is thus called for. An extensive study has been made on the catalytic graphitization of carbon by various metals.[14–26] Among the metal particulates which have been studied, the Pt nanoparticles seem to be more effective in converting the carbon materials into graphites.[17,18]

In this context, we utilized the Pt-ions to implant UNCD films, followed by post-implantation annealing at 600°C, for the purpose of enhancing their electrical conductivity and FEE properties. Importantly, current imaging tunneling spectroscopy (CITS) in scanning tunneling spectroscopy (STS) mode is used to directly examine the increased emission site densities in Pt-ion implanted/annealed UNCD films than the as-implanted UNCD films in nanometer scale. The modifications to the microstructure of these films due to Pt-ion

implantation/annealing processes were investigated in detail using transmission electron microscopy (TEM).

2. Experimental methods

The UNCD films with ultra-smooth surface characteristics at nanoscale were grown on *n*-type silicon substrates in a microwave plasma enhanced chemical vapor deposition system (2.45 GHz, 6″ IPLAS-CYRANNUS-I, Troisdorf, Germany) in a CH_4/Ar = 1/99 sccm plasma excited by 1200 W microwave power under 200 mbar pressure. Prior to the growth of UNCD films, the Si substrates were first thoroughly cleaned by rinsing the Si substrates in a water-diluted hydrogen peroxide/ammonium hydroxide and hydrogen peroxide/hydrochloric acid solution sequentially. Then the cleaned Si substrates were ultrasonicated in methanol solution containing nanodiamond powders (about 4 nm in size) and titanium powders (< 32.5 nm) (SIGMA ALDRICH) for 45 min to facilitate the nucleation of diamond. The growth process was carried out at low substrate temperature without any intentional heating of the substrate. The substrate temperature was estimated to be around 475°C by a thermocouple attached to the substrate holder. The films were grown for 3 h to reach a thickness of 800 nm, which was confirmed from the cross-sectional scanning electron microscopic image (figure not shown). Platinum ion implantation was performed on UNCD films at room temperature with implantation energy of 500 keV and the ion dosages are varied from 1 x 10^{15} to 1 x 10^{17} ions/cm^2 at an ion flux of 1.035 x 10^{12} ions/cm^2/s. The pristine UNCD films are designated as Pt0 and the films which have undergone implantations using ion doses of 1 x 10^{15}, 1 x 10^{16}, 1 x 10^{17} ions/cm^2 are designated as Pt15, Pt16 and Pt17 samples, respectively. Moreover, the Pt17 films were annealed subsequently at 600°C in N_2 gas atmosphere for 30 min and are designated as Pt17A films.

Hall measurements were carried out in a van der Pauw configuration[27] (ECOPIA HMS-3000) to examine the conducting behavior of these films. The excitation current used for four-probe resistance measurements is 0.1 μA and the magnetic field used for mobility measurements is 0.55 T, respectively. The FEE characteristics of the samples were measured using a parallel plate setup, in which the UNCD films (cathode)-to-molybdenum rod (2 mm in diameter, anode) distance was controlled using a micrometer. The field emission currents are recorded at a sequence of gap voltages using an electrometer (Keithley 2410) at high vacuum with a pressure

of 1.3 x 10^{-6} mbar. The current density (J) values were determined by dividing the total current by the area of the anode (Mo rod), whereas the electrical field (E) was designated as the ratio of applied voltage to the cathode-to-anode gap. The current density versus electrical field (J-E) characteristics thus obtained were plotted to check whether the J-E characteristics of the materials followed the Fowler Nordheim (FN) theory.[28]

$$J = \left(\frac{A\beta^2 E^2}{\varphi}\right) \exp\left(-\frac{B\emptyset^{\frac{3}{2}}}{\beta E}\right)$$

where $A = 1.54 \times 10^{-6}$ A eV/V^2 and $B = 6.83 \times 10^9$ eV$^{-3/2}$ V/m, β is the field-enhancement factor, J is the FEE current density, E is the applied field and φ is the work function of the emitting materials. The FEE parameters, turn-on field (E_0), FEE current density (J) and field enhancement factor (β), were extracted from the J-E curves using FN plots, which is $ln\ J/E^2$ vs. $1/E$ curves. Moreover, the FEE behavior was investigated elaborately in a microscopic scale by a combined custom-built non-contact ultrahigh vacuum atomic force microscopy (NC-UHV AFM)/scanning tunneling microscopy (UHV-STM, 150 Aarhus, SPECS GmbH) system, at room temperature with a base pressure of at least 6.6×10^{-10} mbar. For topographic imaging and CITS mapping, we have used electrochemically etched tungsten tips. CITS spectra with voltages ramping from -3.3 to 3.3 V were measured simultaneously, while the STM tips were scan over the sample's surface of the area of 1μm x 1μm.

The surface morphology of the films was investigated by SEM (Joel 6500). The crystalline quality and the depth profile of the UNCD films were characterized by Raman spectroscopy (Lab Raman HR800, Jobin Yvon; λ = 632 nm and spectral resolution = 0.5 cm^{-1}) and secondary ions mass spectroscopy (SIMS; Cameca IMS-4f), respectively. The chemical bonding structures of the films were investigated by X-ray photoelectron spectroscopy (XPS; PHI 1600). The detailed microstructure and the bonding structure of the samples were examined using transmission electron microscopy (TEM, Joel 2100F) and electron energy loss spectroscopy (EELS, Gatan Enfina) in TEM, respectively.

3. Results and discussion

3.1. Material and electrical characteristics

The implantation of Pt-ions (1×10^{17} ions/cm^2) and subsequent annealing induces marked change on the surface microstructure of the UNCD films. While the pristine UNCD films contain equi-axed nano-grain microstructure (Fig. 1a), the Pt-ions implantation/annealing processes rendered the surface morphology of UNCD films to a featureless surface morphology (Fig. 1b). The bonding character of different types of carbon in the UNCD films is characterized by visible-Raman spectroscopy. Fig. 1c shows the visible-Raman spectra of (I) Pt0, (II) Pt17, and (III) Pt17A films, which were deconvoluted by using multi-peak Lorentzian fitting method. Curve I in this figure shows that the Raman spectrum of Pt0 films contains peaks at around 1160 cm^{-1} and 1475 cm^{-1}, which are attributed to the ν_1 and ν_3 modes of *trans*-polyacetylene (*t*-PA) present in the grain boundaries of Pt0 films.[29,30] Broadened peak at around 1340 cm^{-1} (D-band) and 1540 cm^{-1} (G-band), which corresponds to the disordered sp^2 bonded carbon and graphitic phase, respectively, are also observed in Pt0 films.[31,32] A shoulder peak at around 1600 cm^{-1} (G′ band) is seen that possibly arises from the nanocrystalline graphitic content in the films.[31] Raman resonance D′ peak at 1332 cm^{-1} corresponding to sp^3-bonded carbon shows less intensity for Pt0 films, because the visible-Raman spectroscopy is more sensitive to sp^2-bonded carbon as compared to that of sp^3-bonded one.[32] Curve II of Fig. 1c shows the effect of Pt-ion implantation at the fluence of 1×10^{17} ions/cm^2 on altering the bonding characteristics of the UNCD films. It shows higher intensities of D and G peaks, indicating amorphization and graphitization type of transitions. The intensity of the ν_1 and ν_3 bands decreased pronouncedly, in accompanied with slight blue-shifted due to Pt-ion implantation process that is probably a sign of the breaking of *t*-PA chains due to high doses Pt-ion implantation.[29] Post-implantation annealing increased markedly the D- and G-band resonance peak intensity with some blue-shift of G-band (curve III of Fig 1c). The Raman spectra show I_D/I_G values (ratio of intensities of D-peak to G-peak) 0.67, 0.72, and 1.01 for Pt0, Pt17 and Pt17A films, respectively. The increase of the I_D/I_G values implies the formation of nanographite phases and decrease in sp^3 content according to increasing disorder in carbon materials.[32,33]

The SIMS depth profile shown in Fig. 2 suggests that platinum ions are implanted into the UNCD films to a depth of about 400 nm with peak concentration located at around 145 nm

beneath the surface that is in accord with SRIM calculation. This profile confirms that Pt-ions have been implanted in the UNCD films. The Hall measurements were carried out in a van der Pauw configuration. The electrical conductivity of the Pt-ion implanted UNCD films are plotted as closed square symbols in Fig. 3a. While the Pt0 and Pt15 films are too resistive to be measurable, the electrical conductivity of Pt-ion implanted UNCD films increases monotonously with increasing ion dosage, from 0.043 $(\text{ohm-cm})^{-1}$ for Pt16 films to about 21.0 $(\text{ohm-cm})^{-1}$ for Pt17 films. Upon annealing, the conductivity value further increases to about 94.0 $(\text{ohm-cm})^{-1}$ with $n = 3.72 \times 10^{18}$ cm^{-2} and $\mu = 8.4 \times 10^{2}$ $\text{cm}^2/\text{V} \cdot \text{s}$ for Pt17A films (see Table 1).

The effect of Pt-ion implantation/annealing processes in modifying the FEE properties of UNCD films is shown in Fig. 3b with the inset indicating the corresponding FN plots. The Pt-ion implantation/annealing processes improved markedly the FEE properties of the UNCD films that are evidently due to the increase in conductivity of the films. The Pt0 films exhibit the largest E_0 of 22.2 V/μm with the lowest J of 1.26 mA/cm^2 at an applied field of 37.0 V/μm (curve I, Fig. 3b). The E_0 value decreases consistently with the dosage of Pt-ion implantation (curves II–IV) and the post-implantation annealing process further lowers the turn-on field (open circles, Fig. 3a). The Pt17A films show the best FEE characteristics, i.e., the lowest E_0 of 4.17 V/μm and the highest J of 5.08 mA/cm^2 at an applied field of 7.2 V/μm (curve V, Fig. 3b). These FEE parameters are listed in Table I. Notably, the E_0 value is designated as the interception of the high and low-field line segments of the FN plots, viz. the $\ln(J/E^2)$ versus $1/E$ curves (inset of Fig. 3b). Furthermore, the actual β value can be estimated from the equation listed as follows:

$$\beta = [-6.8 \times 10^3 \, \varphi^{3/2}]/m$$

where, m is the slope of the FN plot. From inset of Fig. 3b, a plot of $\ln(J/E^2)$ versus $(1/E)$, the FN plot, gives a straight line. From the slopes of the FN plots the β values of the Pt-ion implanted UNCD samples were calculated by taking the φ value of diamond and Pt as 5.0 eV[34] and 5.65 eV[35], respectively. The Pt0 films exhibit the lowest β value of 560. The β value increases consistently with the dosage of Pt-ion implantation. The post-implantation annealing process further increases the β value to 4075, which is almost 7 times as much that of the Pt0 films. The electrical conductivity and the FEE properties of the UNCD films implanted with other kinds of species were listed in Table 2 to facilitate the comparison.[12,13,36–40] Moreover, we have carried out the life time measurements for Pt17A films, as stability of the field emission current is an

important parameter related to prospective applications of cold cathode materials. Interestingly, the Pt17A films possess good life time stability. The corresponding *J* versus time curve is shown as the inset of Fig. 3a, indicating the emission current variations recorded over a period of 145 min at a working field of 6.8 V/μm, corresponding to *J* of 3.0 mA/cm^2, for Pt17A films. As seen from the figure, no significant discharges or spikes due to emitter adsorbates are produced and the emitted current remains constant over this period of time.

XPS measurements have been carried out for the purpose of understanding how Pt-ion implantation/annealing processes modify the surface chemical bonding characteristics of UNCD films. The C1s photoemission spectra of the Pt0, Pt17 and Pt17A films are shown in Fig. 4. The measurement was conducted without ion sputtering etching to avoid reconfiguration of the surface bondings. The background was subtracted using Shirley's method[41] and the data were fitted with Lorentzian peaks with binding energies at 284.4, 285.1 and 287.0 eV corresponding to sp^2 C=C, sp^3 C-C and C-O/C-O-C bonds, respectively. Their relative intensities are tabulated in Table 3. In Pt0 films (Fig. 4a), sp^3 C-C bonding is predominant with the peak intensity of 58.3% accompanying with sp^2 C=C intensity of 38.4% and C-O/C-O-C peak intensity of 3.3%. After Pt-ion implantation, sp^3 C-C peak intensity decreases to 44.2% and sp^2 C=C peak intensity increases to 53.4%. Upon post-implantation annealing, the sp^3 C-C peak intensity decrease further to 38.1% and sp^2 C=C peak intensity increases further to 60.6%. The increase in sp^2 content upon Pt-ion implantation/annealing is consistent with our Raman results (cf. Fig. 1c).

3.2. Scanning tunneling spectroscopy

The local FEE properties of the Pt0, Pt17 and Pt17A films were investigated by CITS mode in STS to directly reveal the distribution of the emission sites in these films. It should be noted that the Pt0 films are too resistive to be investigated by STM measurements. Therefore, the surface of Pt0 film were sputter etched *in-situ* with Ar^+ ions for 1 min to remove nearly 1 nm of surface layer so as to render the Pt0 films conducting enough for STM measurements. Fig. 5a shows the STM image of Pt0 film surface, revealing that the films contain cauliflower like aggregates, which are presumably the coalescence of small diamond grains of about 3 and 5 nm. The current image tunneling spectroscopy (CITS) corresponding to Fig. 5a taken at a sample bias of -3.0 V is shown in Fig. 5b. Bright contrast in the CITS image represents better electron emission. The typical grains and grain boundaries are marked as 'G' and 'GB', respectively, in

Fig. 5a and 5b. Bright and dark regions in CITS image are visible with their shapes having similar geometry with the shapes of grain boundaries (GB) and grains (G) of the STM image, respectively. The CITS image in Fig. 5b shows clearly that the emission sites are mainly located along the boundaries of diamond aggregates.

Fig. 5c and 5e show the high resolution STM (HRSTM) image of Pt17 and Pt17A films, respectively. The grains are also of nanometer size and the rms roughness is found to be ~0.4–0.6 nm. Fig. 5d and 5f show the CITS image corresponding to Fig. 5c and 5e, respectively, taken at a sample bias of -3.0 V, where, again, the bright spots represent large emission current. Bright and dark regions in CITS image are visible with their shapes having resemblance with the shapes of GB and G of the HRSTM image. The CITS images depicted in Fig. 5d and 5f show evidently that the electrons are predominantly emitted from the GBs (bright regions) rather than grains. It is to be noted that some clusters in Pt17 and Pt17A films also emit as like the emission from the GBs. The TEM microstructural investigation, which will be discussed shortly, suggested that these highly emitting clusters could be the carbon-coated Pt nanoparticles which are residually present on the surface of the Pt17 and Pt17A films and are thus marked as 'Pt' in Fig. 5d and 5f. In comparison with the CITS images of Pt0 and Pt17 films, it is clearly evident that the emission sites (bright regions) are more abundant for Pt17A films. Moreover, CITS mapping in Fig. 5d shows that the emission sites at the grain boundaries of Pt17 films is not continuous. In contrast, the CITS mapping of Pt17A films is Fig. 5f depicts that the grain boundaries form interconnected bright emitting sites in Pt17A films such that the electrons can travel easily and emit from these conducting grain boundary sites. However, Raman spectra, XPS and CITS (STS) measurements cannot clearly account for the source of modification on the electrical properties of diamond films due to Pt-ion implantation/annealing processes. TEM microstructural investigation is needed for better understanding the genuine factor that modifies the electrical properties of these films, which will be discussed in detail shortly.

Moreover, the better emission properties observed by CITS mapping in Fig. 5f for Pt17A films are further crosschecked by local current-voltage (I-V) characteristic curves. Fig. 6 shows the local I-V curves taken from STM at various local positions of grains and grain boundaries corresponding to the STM images shown in Fig. 5e for Pt17A films. Only the negative portion of the I-V curves, which indicated the emission of electrons from the films, was shown here.

Reproducible I-V curves were recorded during the scanning. Fig. 6 shows about ten I-V curves in each measurement (open symbols) and the average of these curves was plotted as solid symbols. We observed a significant difference in the I-V characteristic curves at grains and grain boundaries for Pt17A films. The grain boundaries of Pt17A films [curve II (solid star symbols), Fig. 6] emit electrons at a lower threshold bias as compared to that of the grains of Pt17A films [curve I (solid circle symbols), Fig. 6]. Additionally, the Pt residuals presence on the surface of Pt17A films, marked as 'Pt' in the CITS image of Fig. 5f, also showed lower threshold bias [curve III (solid triangle symbols), Fig. 6] as like the grain boundaries of Pt17A films.

3.3. Transmission electron microscopy

The STS measurements clearly illustrate the benefit of Pt-ion implantation/annealing processes on increasing the number density of field emission sites for UNCD films. However, the authentic cause for such an effect is still not clear. It is expected that the modification on the granular structure for these films due to Pt-ion implantation/annealing processes is the key. To investigate the possible cause of such phenomena, the detailed microstructure of these films was examined using TEM. Fig. 7 shows the bright field (BF) TEM microstructure of Pt0, Pt17, and Pt17A films with the corresponding selected area electron diffraction (SAED) pattern shown as insets. The Pt0 films contain nano-sized clusters, which are uniformly distributed (Fig. $7a_I$). The corresponding SAED pattern (inset, Fig. $7a_I$) contains sharp diffractions rings corresponding to (111), (220) and (311) diamond lattices, which confirms that the nano-sized clustered are of diamond structure. There is no other diffraction ring than diamond observable. Moreover, there appears diffused ring in the center of SAED, indicating the existence of the sp^2-bonded carbon (graphitic or *a-C* phase), which is presumably located in the grain boundaries of the films. The distribution of the phase constituents in these materials is best illustrated by the composed dark field (c-DF) image (Fig. $7a_{II}$), which is the superposition of several dark field images corresponding to different portion of SAED (indicated in Fig. $7a_{II}$). The high resolution TEM (HRTEM) micrograph shown in Fig. 8 reveals the structure image of region 'A' in Fig. $7a_I$. The Fourier transformed diffractogram of the whole structure image (FT_{0a}, Fig. 8) shows the existence of spotted diffraction pattern arranged in rings, the $(111)_D$, which corresponds to randomly oriented diamond grains (D), and the diffused ring located at the center, which matches up to *a-C* (or nanographitic) phase. The ft_1 image of the designated region '1' and the ft_2 image

corresponding to the region '2', highlight the presence of diamond and *a-C* phase, respectively. The large diamond grains seem to be the agglomeration of small diamond grains.

BF TEM image in Fig. $7b_I$ shows that Pt-ion implantation induced dramatic modification on the granular structure of the UNCD films (the Pt17 films). The large diamond aggregates, which frequently occurred to Pt0 films, are no longer observable, implying that the incident Pt-ions have disintegrated the aggregates, implying that the aggregates occurred in Pt0 films are soft agglomerates. Moreover, Fig. $7c_I$ shows that post-implantation annealing renders the nano-sized particulates contained in the UNCD films are larger in size and are more sharply defined (Fig. $7c_I$). The SAED pattern for Pt17 films (inset, Fig. $7b_I$) reveals that, besides the presence of strong diffraction rings corresponding to (111), (220) and (311) diamond lattice planes, there is a diffraction ring located outside the (111) diamond ring, which corresponds to Pt material with lattice spacing of 0.23 nm.[42] Interestingly, there appears an faint extra diffraction ring of smaller size than the $(111)_D$ ring, which corresponds to the *i-carbon* (*i-C*), the bcc structured carbon with a_0=0.432 nm.[43,44] In contrast, the SAED pattern for Pt17A films (inset, Fig. $7c_I$) shows that these films also contain randomly oriented diamond and Pt particulates (~5 nm in size). However, unlike that observed for the Pt17 films, no extra diffraction ring corresponding to *i-C* phase was detected in the SAED pattern of Pt17A films. Both the SAED of Fig. $7b_I$ and $7c_I$ contain a prominent diffused ring in the center, indicating the existence of some sp^2-bonded carbon in the Pt17 and Pt17A films. The intensity of central diffused ring is much higher in Pt17A films (cf. inset of Fig. $7c_I$) compared with that in Pt17 films (cf. inset of Fig. $7b_I$), implying that the post-implantation annealing process induced large proportion of sp^2-bonded carbon. Again, the distribution of phase constituents in these materials is illustrated in c-DF image (Fig. $7b_{II}$ and $7c_{II}$).

Detailed investigations were carried out for Pt17 films (region 'B', Fig. $7b_I$) and Pt17A films (region 'C', Fig. $7c_I$) and the corresponding HRTEM image are shown in Figs. 9 and 10, respectively. The FT images of the whole structure image (FT_{0b} in Fig. 9 and FT_{0c} in Fig. 10) contain spotted diffraction pattern arranged in a ring geometry, revealing the existence of nano-sized particulates, and the diffused ring, indicating the presence of the *a-C* (or graphitic) phase. Notably, the FT_{0b} image corresponding to Pt17 films (inset, Fig. 9) contains more complicated diffraction spot patterns than the FT_{0c} image corresponding to Pt17A films (inset, Fig. 10). The

FT_{0b} image shows the existence of the outer ring of $(111)_D$ diamond (D) and the inner ring of *i-C* phase. The diffraction spots correspond to Pt phase are sparsely distributed along a ring outside the $(111)_D$ ring. In contrast, the FT_{0c} image shows only the diffraction spots related to diamond and Pt particulates with the later of much larger intensity. The inner ring corresponds to *i-C* phase is no longer observable. In Fig. 9, the presence of diamond, Pt, *i-C* and sp^2-bonded carbon phases in Pt17 films are highlighted by region '3' (ft_3), region '4' (ft_4), region '5' (ft_5) and region '6' (ft_6), respectively, whereas, in Fig. 10, the coexistence of diamond and Pt clusters in Pt17A films are highlighted by region 7 (ft_7), region 8 (ft_8), respectively. Furthermore, the ft_9-image in Fig. 10 highlights that the Pt-clusters shown in region 9 were aggregated due to post-implantation annealing process and were encased with a thin graphitic phase.

The modification on microstructure of UNCD films due to these processes is best illustrated by the linear diffraction patterns (LDP), which are derived from the SAED indicated in Fig. 7a–c and are shown in Fig. 11. These LDP patterns reveal that while the Pt0 films (curve I, Fig. 11) contain mainly the diamond, the Pt17 films contain an extra diffraction peak corresponding to Pt, along with the presence of *i-C* phases (curve II, Fig. 11). Post-implantation annealing results in the conversion of *i-C* phases into graphitic phases (curve III, Fig. 11) that will be more clearly evidenced by the EELS investigations. Based on these TEM investigations, it is obvious that Pt-ion implantation/annealing processes induced the formation of sp^2-bonded carbon (graphitic or *a-C* phase) and *i-C* phase, whereas the subsequent annealing process converted these phases into graphitic one that is in concurrence with the Raman and the XPS investigations.

Further, selective area EELS spectra (Fig. 12) were recorded in the carbon K-edge region to unambiguously distinguish between the diamond and the non-diamond phases contained in the Pt-ion implanted/annealed UNCD films.[45] Fig. 12 shows the selected area EELS spectra corresponding to each BF TEM micrograph in Fig. 7, revealing the marked changes in bonding structures due to Pt-ion implantation/annealing processes. Curve I in Fig. 12a shows the core-loss EELS spectrum of Pt0 films, corresponding to BF TEM image in Fig. 7a, which exhibit typical EELS spectrum of diamond with Fd3m structure, as they contain a abrupt rise in σ*-band (near 290 eV) and a deep valley near 302 eV.[5,46] The core-loss EELS spectra of Pt17 and Pt17A films (curves II and III, Fig. 12a) also contain σ*-band and a deep valley, which is essentially the same as those of the Pt0 films, except there presence a π*-band at 284.5 eV in core-loss EELS

spectra of Pt17 and Pt17A films (curves II and III, Fig. 12a), indicating the induction of some proportion of sp^2-bonded carbon due to Pt-ion implantation/annealing processes. The π*-band is of larger intensity for Pt17A films, compared with those of Pt17 films, indicating the containment of larger proportion of sp^2 bonded carbon in Pt17A films.

Now the question yet to be solved is what is the nature of grain boundary phases (*a-C* or graphite) induced when the UNCD films were implanted with Pt-ions and subsequently post-annealed. It should be mentioned that the plasmon-loss EELS spectra is the most effective measurement to differentiate the crystalline sp^2-bonded carbons (the graphite) from the amorphous one, as the plasmon-loss EELS spectra for the graphitic phase shows a prominent peak at s_3 (27 eV) and the *a-C* phase shows a peak at s_1 (22 eV),[5,46] whereas the crystalline sp^3-bonded carbons, the diamond, shows a peak corresponding to the bulk plasmon loss at s_4 (33 eV) with a shoulder corresponding to the surface plasmon loss at s_2 (23 eV). The I_{s2}/I_{s4} ratio is about 1:√2. Fig. 12b shows the selected area plasmon-loss EELS spectra of the same regions as those for core-loss EELS. It is observed that the Pt0 films (curve I, Fig. 12b) contains s_2 and s_4 peaks, indicating that Pt0 films are predominantly diamond.[46] The containment of sp^2-bonded carbon is minimal in Pt0 films. Curve II in Fig. 12b, which corresponds to Pt17 films, is predominated with s_1-band (22 eV) with very small proportion of the s_2-band (at 23 eV) and s_4-band (at 33 eV). The emergence of s_1-band indicates that some of the materials in Pt17 films were transformed into *a-C* phases. Quite the opposite, the plasmon-loss spectrum for Pt17A films (curve III, Fig. 12b) is predominated by s_3-band (~27 eV) with the s_2- and s_4-bands of much smaller intensity, indicating that the sp^2-bonded carbon (π*-band) implied by core-loss EELS (cf. curve III, Fig. 12a) is nanographitic phase rather than amorphous carbon. On the basis of EELS and TEM investigations, it is noticed that Pt-ion implantation/annealing processes induced the formation of nanographitic phases, which is in concurrence with the Raman and the XPS investigations.

The mechanism, by which the Pt-ion implantation/annealing process enhanced the conductivity and FEE properties of UNCD films, can be accounted for by the catalytic graphitization of the sp^2-bonded carbon located along the grain boundaries of the films, as previous studies observed that the incorporation of metals into carbon films can act as catalysts in the conversion of sp^3 to sp^2 content and, upon heat treatment, induced the graphitization of *a-C*.[14–26] The formation of nanographitic phase, surrounding the nano-sized diamond grains of the

UNCD films resulted in interconnected conduction network enriching the electrical conductivity and the FEE properties of UNCD films.[48] The conversion of non-conducting *i-C* and *a-C* phases at the grain boundaries of Pt17 films to conducting graphitic phases has significant effect on increasing the electron emission sites in Pt17A films (cf. Fig. 5f). Restated, the Pt-ion implantation constructively formed the Pt nanoparticles in the UNCD films and catalytically induced the formation of nanographitic phases in the periphery of Pt nanoparticles on the subsequent annealing process. The electrons can transport easily through the nanographitic phases to the emitting surface and are then emitted to vacuum without any difficulty. Consequently, the formations of Pt nanoparticles due to Pt-ion implantation and the catalytic activity of Pt nanoparticles in inducing the nanographitic phases due to annealing are the genuine factors for the superior FEE properties of the Pt17A films.

4. Conclusions

In summary, we have demonstrated a feasible way of fabricating highly conducting UNCD films via the Pt-ion implantation/annealing processes, which markedly modified the microstructure and the FEE properties of the films. The implanted Pt-ions first form uniformly distributed Pt nanoparticles, which catalytically induced the formation of nanographitic phases in Pt17A films due to annealing at 600°C. The nanographites contained in the grain boundaries of Pt17A films form highly conductive channels for the films. CITS in STM analyses revealed that these channels give rise to prominent field emission sites in the grain boundaries, resulting in high electrical conductivity and enhanced FEE properties for the Pt17A films. The synthesis of highly conducting Pt17A films with better FEE characteristics open up a pathway to the next generation of electron field emitters for the applications in the high-definition flat panel displays or plasma illumination devices.

Acknowledgements

The authors like to thank the financial support of National Science Council, Taiwan through the project nos. NSC 101-221-E-007-064-MY3 and MOST 103-2112-M-032-002.

Notes and References

[a]*Department of Materials Science and Engineering, National Tsing-Hua University, Hsinchu 300, Taiwan, R.O.C.*

Email: nhtai@mx.nthu.edu.tw

[b]Graduate School of Engineering, Osaka University, Osaka 565-0871, Japan.

[c]*Materials Science Group, Indira Gandhi Centre for Atomic Research, Kalpakkam 603 102, India.*

[d]*Department of Physics, Tamkang University, Tamsui 251, Taiwan, R.O.C.*

Email: inanlin@mail.tku.edu.tw

1 T. D. Corrigan, D. M. Gruen, A. R. Krauss, P. Zapol and R. P. H. Chang, *Diamond Relat. Mater.*, 2002, **11**, 43.

2 J. Birrell, J. A. Carlisle, O. Auciello, D. M. Gruen and J. M. Gibson, *Appl. Phys. Lett.*, 2002, **81**, 2235.

3 D. Zhou, A. R. Krauss, L. C. Qin, T. G. McCauley, D. M. Gruen, T. D. Corrigan, R. P. H. Chan and H. Gnaser, *J. Appl. Phys.*, 1997, **82**, 4546.

4 J. Birrell, J. E. Gerbi, O. Auciello, J. M. Gibson, D. M. Gruen and J. A. Carlisle, *J. Appl. Phys.*, 2003, **93**, 5606.

5 R. Arenal, P. Bruno, D. J. Miller, M. Bleuel, J. Lal and D. M. Gruen, *Phys. Rev. B*, 2007, **75**, 195431.

6 K. J. Sankaran, J. Kurian, H. C. Chen, C. L. Dong, C. Y. Lee, N. H. Tai and I. N. Lin, J. *Phys. D: Appl. Phys.*, 2012, **45**, 365303.

7 S. Bhattacharyya, O. Auciello, J. Birrell, J. A. Carlisle, L. A. Curtiss, A. N. Goyette, D. M. Gruen, A. R. Krauss, J. Schlueter, A. Sumant and P. Zapol, *Appl. Phys. Lett.*, 2001, **79**, 1441.

8 Y. C. Lin, K. J. Sankaran, Y. C. Chen, C. Y. Lee, H. C. Chen, I. N. Lin and N. H. Tai, *Diam. Relat. Mater.*, 2011, **20**, 191.

9 R. Kalish, *Carbon*, 1999, **37**, 781.

10 S. Talapatra, J. Y. Cheng, N. Chakrapani, S. Trasobares, A. Cao, R. Vajtai, M. B. Huang and P. M. Ajayan, *Nanotechnology*, 2006, **17**, 305.

11 S. Prawer and R. Kalish, *Phys. Rev. B*, 1995, **51**, 15711.

12 X. J. Hu, J. S. Ye, H. J. Liu, Y. G. Shen, X. H. Chen and H. Hu, *J. Appl. Phys.*, 2011, **109**, 053524.

13 X. J. Hu, J. S. Ye, H. Hu, X. H. Chen and Y. G. Shen, *Appl. Phys. Lett.*, 2011, **99**, 131902.

14 W. Lu, K. Komvopoulos and S.W. Yeh, *J. Appl. Phys.*, 2001, **8**9, 2422.

15 Qi G J, Zhang S, Tang T T, Li J F, Sun X W and Zeng X T. *Surf Coat Tech* 2005, **198**, 300.

16 K. Bewilogua, R. Wittorf, H. Thomsen and M. Weber, *Thin Solid Films*, 2004, **447**, 142.

17 Y. V. Pleskov, Y. E. Evstefeva and A. M. Baranov, *Diamond Relat. Mater.*, 2002, **11**, 1518.

18 N. W. Khun, E. Liu, G. C. Yang, W. G. Ma and S. P. Jiang, *J Appl Phys*, 2009, **106**, 013506.

19 C. S. Lee, T. Y. Kim, K. R. Lee and K. H. Yoon, *Thin Solid Films*, 2004, **447**, 169.

20 H. Hofsass, H. Feldermann, R. Merk, M. Sebastian and C. Ronning, *Appl. Phys. A*, 1998, **66**, 153.

21 A. Oya and S. Otani, *Carbon*, 1979, **17**, 131.

22 C. Corbella, E. Bertran, M. C. Polo, E. Pascual and J. L. Andujar, *Diamond Relat. Mater.*, 2007, **16**, 1828.

23 J. Robertson, *Mater. Sci. Eng.*, *R* 2002, **37**, 129.

24 C. Corbella, G. Oncins, M. A. Gomez, M. C. Polo, E. Pascual, J. G. Céspedes, J. L. Andújar and E. Bertran, *Diamond Relat. Mater.*, 2005, **14**, 1103.

25 C. Strondl, N. M. Carvalho, J. T. M. DeHosson and G. J. van der Kolk, *Surf. Coat. Technol.*, 2003, **162**, 288.

26 G. J. Qi, S. Zhang, T. T. Tang, J. F. Li, X. W. Sun, X. T. Zeng, *Surf. Coat. Technol.*, 2005, **198**, 300.

27 G. Rietveld, C. V. Koijmans, L. C. A. Henderson, M. J. Hall, S. Harmon, P. Warnecke, B. Schumacher, *IEEE Transactions on instrumentation and measurements*, 2003, **52**, 449.

28 R. H. Fowler and L. Nordheim, *Proc. R. Soc. London, Ser. A*, 1928, **119**, 173.

29 Z. Sun, J. R. Shi, B. K. Tay and S. P. Lau, *Diamond Relat. Mater.*, 2000, **9**, 1979.

30 A. C. Ferrari and J. Robertson, *Phys. Rev. B*, 2001, **63**, 121405.

31 J. Michler, Y. Von Kaenel, J. Stiegler and E. Blank, *J. Appl. Phys.*, 1998, **81(1)**, 187.

32 A. C. Ferrari and J. Robertson, *Phys. Rev. B*, 2000, **61**, 14095.

33 A. Ilie, A. C. Ferrari, T. Yagi, S. E. Rodil, J. Robertson, E. Barborini and P. Milani, *J. Appl. Phys.* 2001, **90**, 2024.

34 J. Liu, V. V. Zhirnov, A. F. Myers, G. J. Wojak, W. B. Choi, J. J. Hren, S. D. Wolter, M. T. McClure, B. R. Stoner, J. T. Glass, *J. Vac. Sci. Technol. B* 1995, **13(2)**, 422.

35 Y. Feng, H. Liu, P. Wang, F. Ye, Q. Tan, J. Yang, *Scientific Reports* 2014, **4**, 1.

36 W. Zhu, G. P. Kochanski, S.Jin, *Science* 1998, **282**, 1471.

37 K. J. Sankaran, Y. F. Lin, W. B. Jian, , H. C. Chen, K. Panda, B. Sundaravel, C. L. Dong, N. H. Tai, I. N. Lin, *ACS Appl. Mater. Interfaces* 2013, **5**, 1294.

38 J. P. Thomas, H. C. Chen, N. H. Tai, I. N. Lin, *ACS Appl. Mater. Interfaces* 2011, **3**, 4007.

39 K. J. Sankaran, H. C. Chen, B. Sundaravel, C. Y. Lee, N. H. Tai and I. N. Lin, *Appl. Phys. Lett.*, 2013, **102**, 061604.

40 K. J. Sankaran, K. Panda, B. Sundaravel, N. H. Tai and I. N. Lin, *J. Appl. Phys.* 2014, **115**, 063701.

41 Y. F. Chen, *Surf. Sci.*, 1997, **380**, 199.

42 Z. Peng, F. Somodi, S. Helveg, C. Kisielowski, P. Specht and A. T. Bell, *J. Catalysis*, 2012 **286**, 22.

43 H. Hirai and K. Kondo, *Science*, 1991, **253**, 722.

44 P. Kovarik, E. B. D. Bourdon and R. H. Prince, *Phys. Rev. B*, 1993, **48**, 12123.

45 A. Dato, V. Radmilovic, Z. Lee, J. Philips and M.Frenklach, *Nano. Lett.*, 2008, **8**, 2012.

46 D. M. Gruen, S. Liu, A. R. Krauss, J. Luo and X. Pan, *Appl. Phys. Lett.*, 1994, **64 (12)**, 1502.

47 P. Kovarik, E. B. D. Bourdon and R. H. Prince, *Phys. Rev. B*, 1993, **48**, 12123.

48 K. J. Sankaran, H. C. Chen, C. Y. Lee, N. H. Tai and I. N. Lin, *Appl. Phys. Lett.*, 2012, **101,** 241604.

Table 1. Electrical and field electron emission properties of platinum ion implanted UNCD films.

Samples	Sheet carrier concentration (cm^{-2})	Mobility ($cm^2/V \bullet s$)	Conductivity $(\Omega \bullet cm)^{-1}$	Turn-on field (V/μm)	FEE current density (mA/cm^2)	Field enhancement factor
Pristine UNCD	---	---	---	22.2	1.26@ 7.2 37.0 V/μm	560
Pt15	---	---	---	15.7	1.84@ 26.3 V/μm	1020
Pt16	5.3×10^{15}	4.4×10^{1}	0.04	9.84	2.33@ 15.3 V/μm	3205
Pt17	2.4×10^{17}	9.7×10^{1}	21	6.88	4.28@ 11.07 V/μm	3745
Pt17A	3.7×10^{18}	8.4×10^{2}	94	4.17	5.08@ 7.2 V/μm	4075

Table 2. Comparison on electrical and field electron emission properties of platinum ion implanted UNCD films with other kind of species in diamond films.

Samples	Sheet carrier concentration (cm^{-2})	Mobility ($cm^2/V \cdot s$)	Conductivity $(\Omega \cdot cm)^{-1}$	Turn-on field (V/μm)	FEE current density (mA/cm^2)	Field enhancement factor
O-implanted UNCD[12]	10^{16}	11	33.3	---	---	---
P-implanted UNCD[13]	10^{17}	143	0.09	---	---	---
H-treated diamond[36]	---	---	---	1.5	1 μA/cm² @ 1.5 V/μm	---
N-doped UNCD[37]	2×10^{22}	---	185	6.13	3.36 @ 8.8 V/μm	---
Li-doped UNCD[38]	3.6×10^{13}	---	7.4×10^{-3}	12	0.20 @ 20.0 V/μm	---
Cu ion implanted UNCD[39]	1.3×10^{14}	0.3×10^{2}	0.07	7.9	2.86@ 13.8 V/μm	---
Au ion implanted UNCD[40]	5.5×10^{20}	8.5×10^{2}	186	4.5	6.70@ 7.8 V/μm	---
Pt17A[Present study]	3.7×10^{18}	8.4×10^{2}	94	4.17	5.08@ 7.2 V/μm	4075

Table 3. Relative intensities of various components of C1s XPS spectra for pristine UNCD and Pt-ion implanted and post annealed UNCD films.

Samples	Chemical bonding (%)		
	sp^2 C=C (284.2 eV)	sp^3 C-C (285.1 eV)	CO/C-O-C (287.0 eV)
Pt0	38.4	58.3	3.3
Pt17	53.4	44.2	2.4
Pt17A	60.6	38.1	1.3

Figure captions

Figure 1. (a) and (b) SEM images of Pt0 films and Pt17A films. (c) visible-Raman spectra of I. Pt0, II. Pt17 and III. Pt17A films taken with 632 nm laser beam.

Figure 2. SIMS depth profiles of C, Pt, and Si species in Pt-ion implanted/annealed (Pt17A) films.

Figure 3. (a) Variation in the electrical conductivity (solid squares) and turn-on field (open circles) against the dosage of Pt-ions implanted in UNCD films with the inset showing the life time measurement, i.e., current density versus time curve of Pt17A sample. (b) The field electron emission properties of various dosage of Pt-ion implanted and annealed UNCD films. The inset of (b) shows the corresponding Fowler Nordheim (FN) plot.

Figure 4. C1s XPS spectra of (a) Pt0, (b) Pt17 and (c) Pt17A films.

Figure 5. The STM image of (a) Pt0 and (b) showing the CITS image corresponding to (a); the HRSTM images of (c) Pt17 and (e) Pt17A films with (d) and (f) showing the corresponding CITS images. The CITS images were acquired at a sample bias of -3.0 V.

Figure 6. Local I-V characteristic curves at the (I) grain (G, solid circle symbols), (II) grain boundary (GB, solid star symbols) and (III) Pt nanoparticles (Pt, solid triangle symbols) of Pt17A films. The reproducible I-V spectra (10 each) are shown by open symbols and the average of these curves is plotted as solid symbols).

Figure 7. (a_I, b_I, c_I) Bright field and (a_{II}, b_{II}, c_{II}) composed dark field TEM images of Pt0, Pt17 and Pt17A films with their corresponding SAED patterns shown as insets.

Figure 8. HRTEM image of Pt0 films corresponding to the region 'A' of Fig. 7a_I. The insets (FT_{0a}) shows the Fourier-transformed image corresponding to the whole structure image, whereas ft_1 and ft_2 images show the FT images corresponding to regions '1' and '2', respectively.

Figure 9. HRTEM image of Pt17 films corresponding to the region 'B' of Fig. $7b_I$. The insets, (FT_{0b}) shows the Fourier-transformed image corresponding to the whole structure image, whereas ft_3 to ft_6 images show the FT images corresponding to regions '3'–'6', respectively.

Figure 10. HRTEM image of Pt17A films corresponding to the region 'C' of Fig. $7c_I$. The insets, (FT_{0c}) shows the Fourier-transformed image corresponding to the whole structure image, whereas ft_7 to ft_9 images show the FT images corresponding to regions '7'–'9', respectively.

Figure 11. The linear diffraction patterns (LDP) derived from the SAED patterns shown in Fig. 7, corresponding to (I) Pt0, (II) Pt17, and (III) Pt17A films, respectively.

Figure 12. Selected area EELS spectroscopy of UNCD films: (a) core-loss EELS spectra and (b) plasmon-loss EELS spectra, where (I) is Pt0, (II) is Pt17, and (III) is Pt17A films.

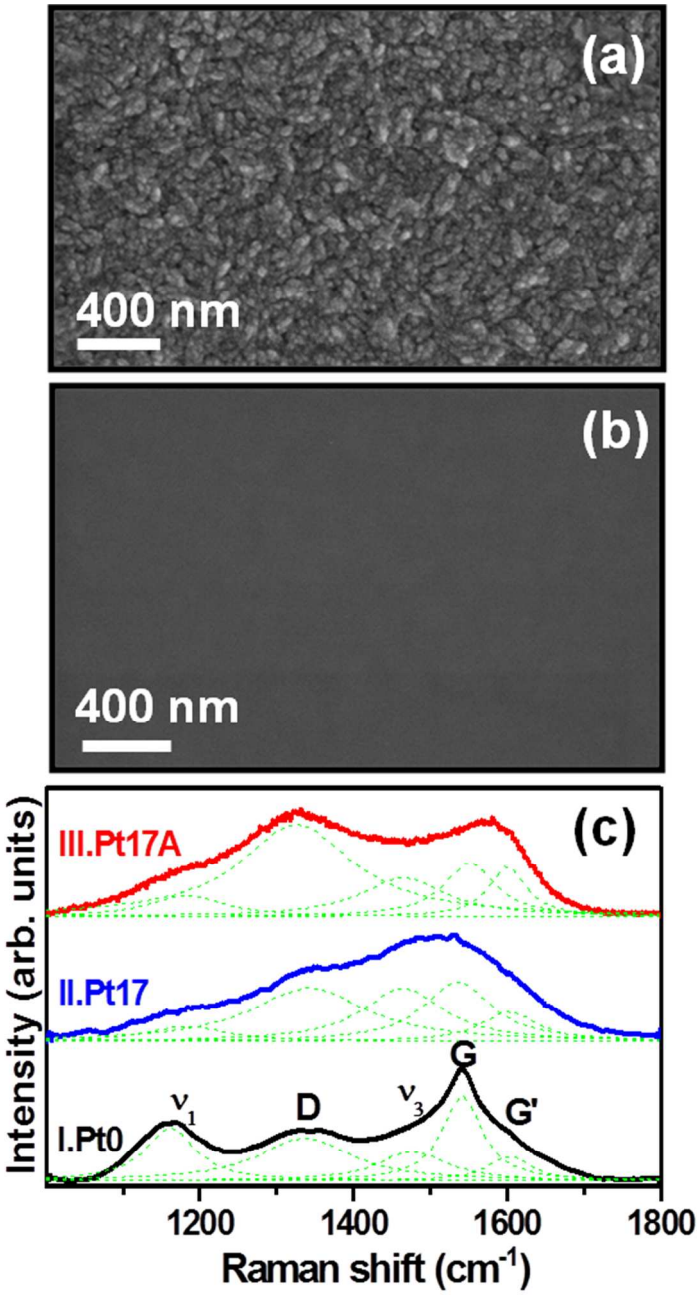

Figure 1

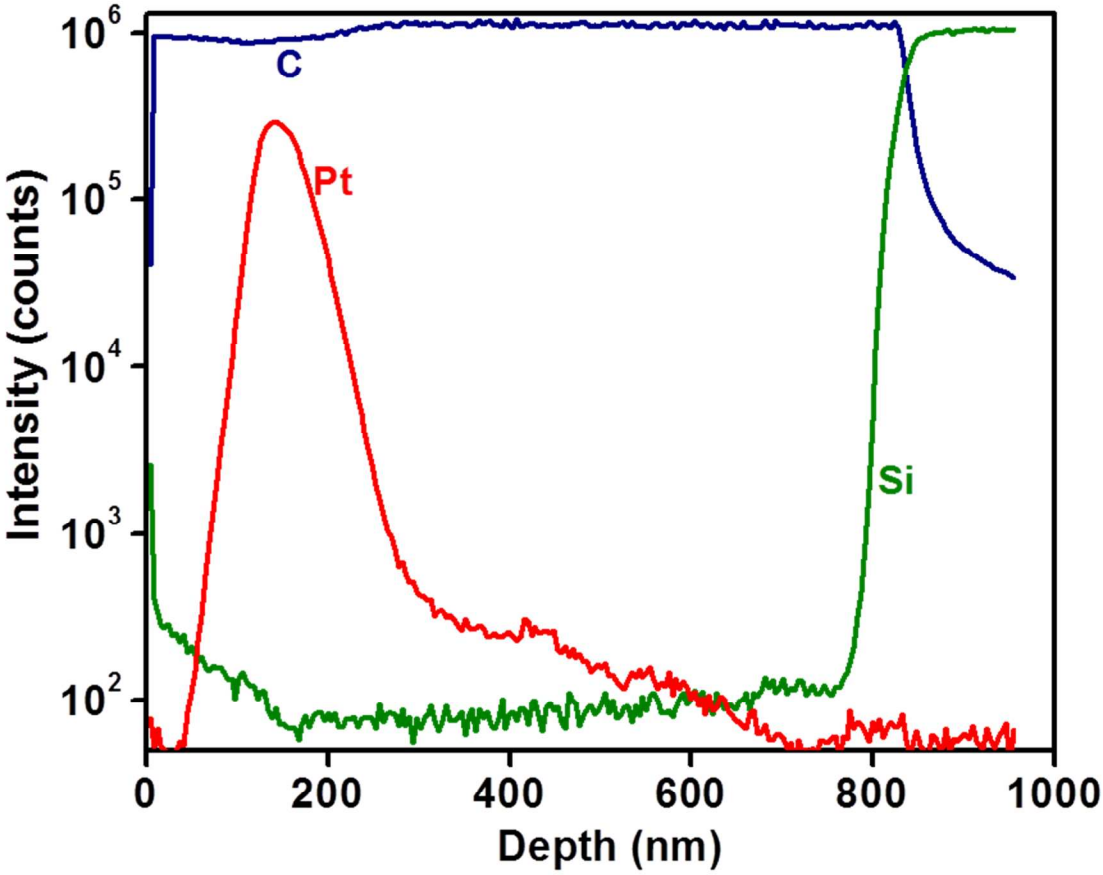

Figure 2

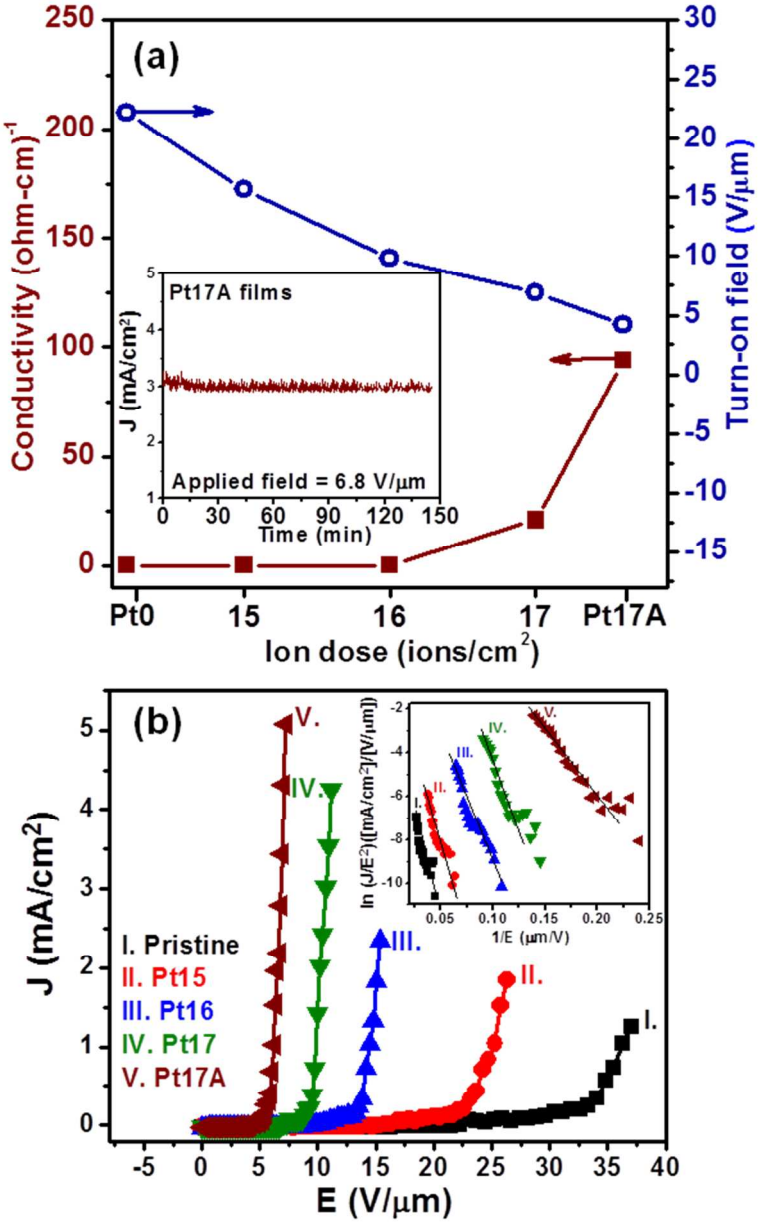

Figure 3

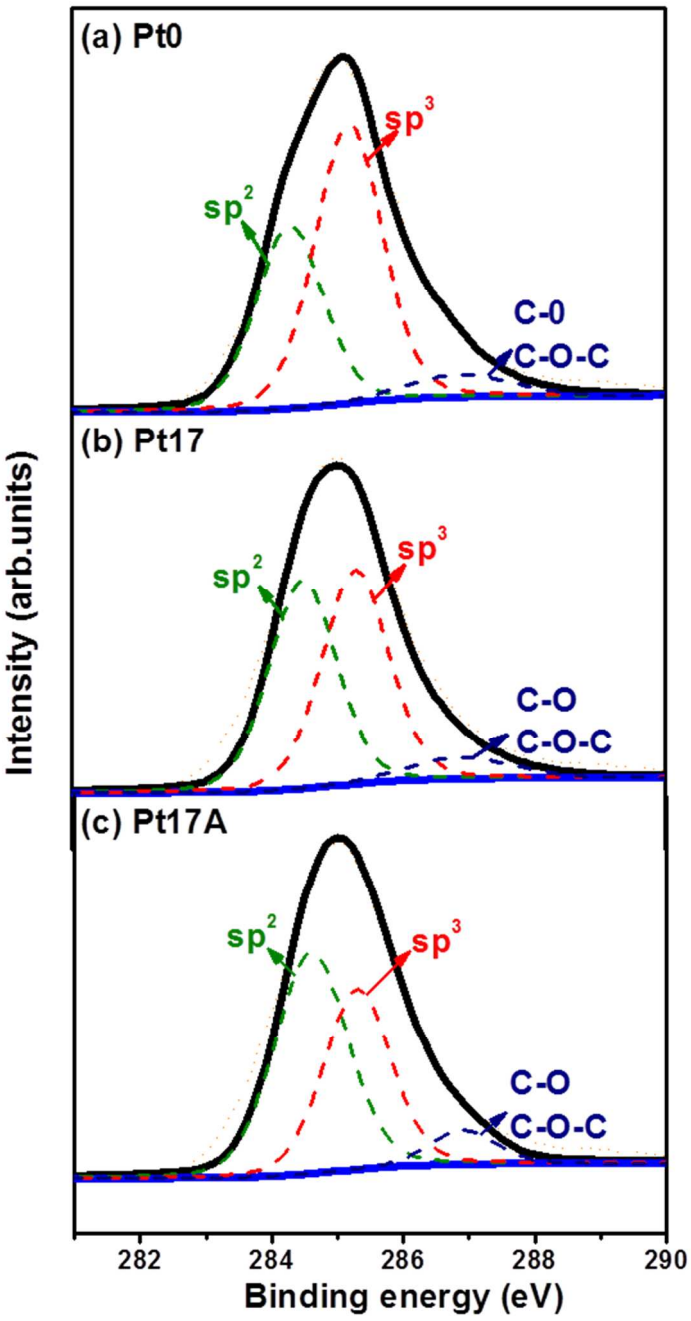

Figure 4

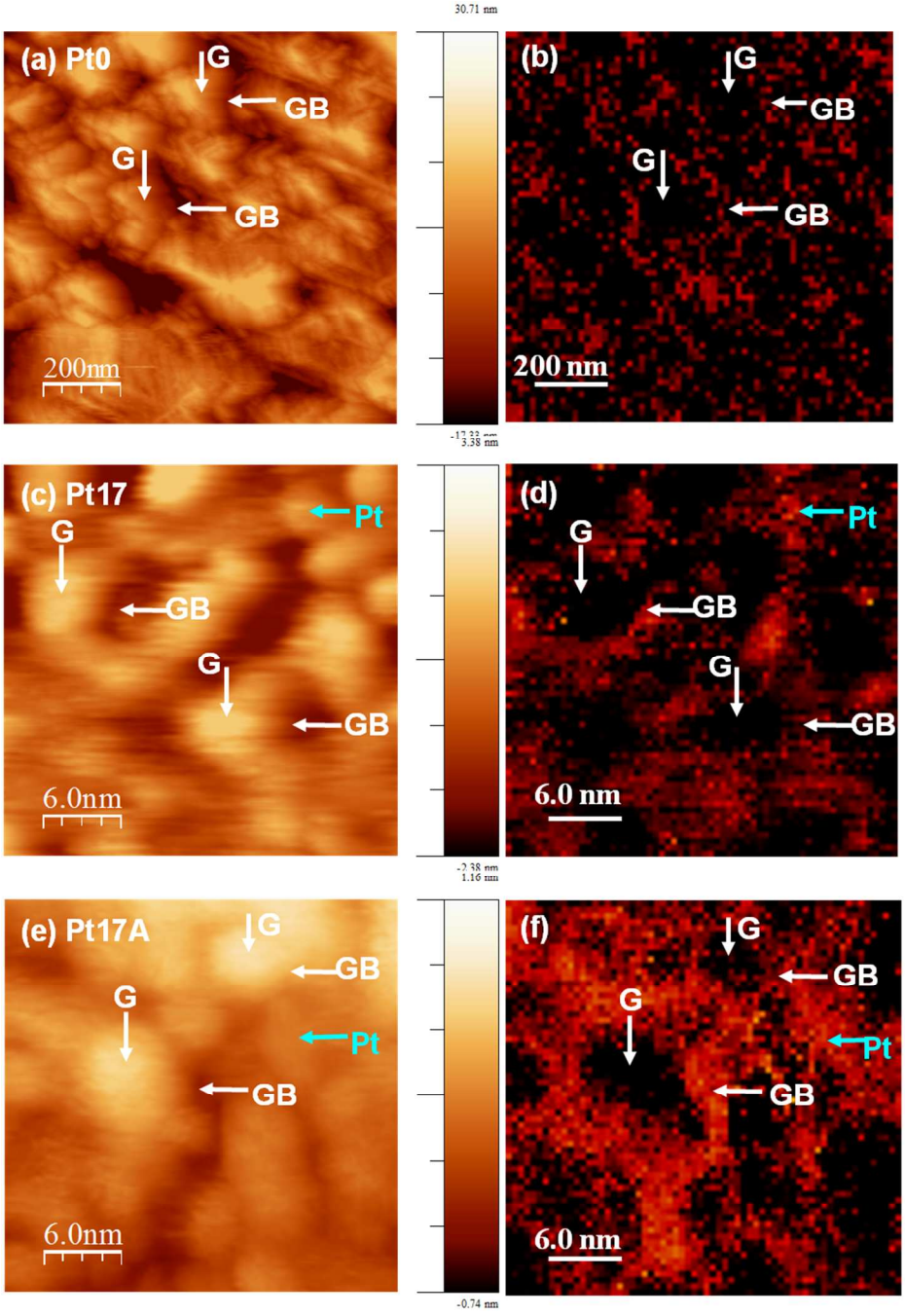

Figure 5

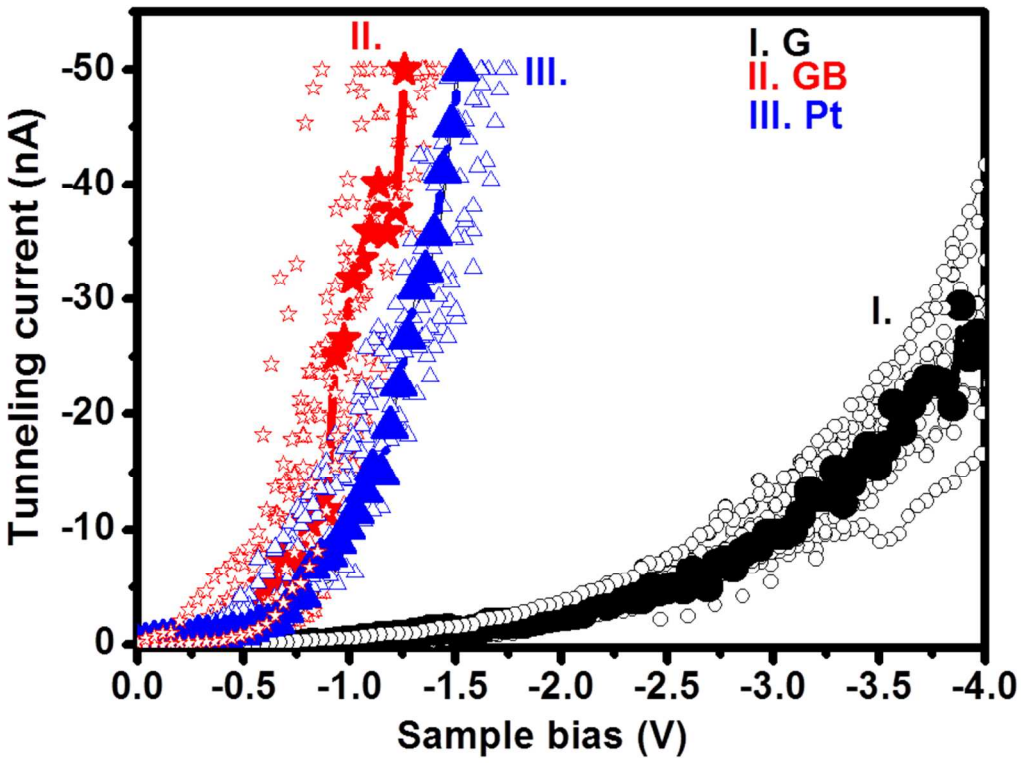

Figure 6

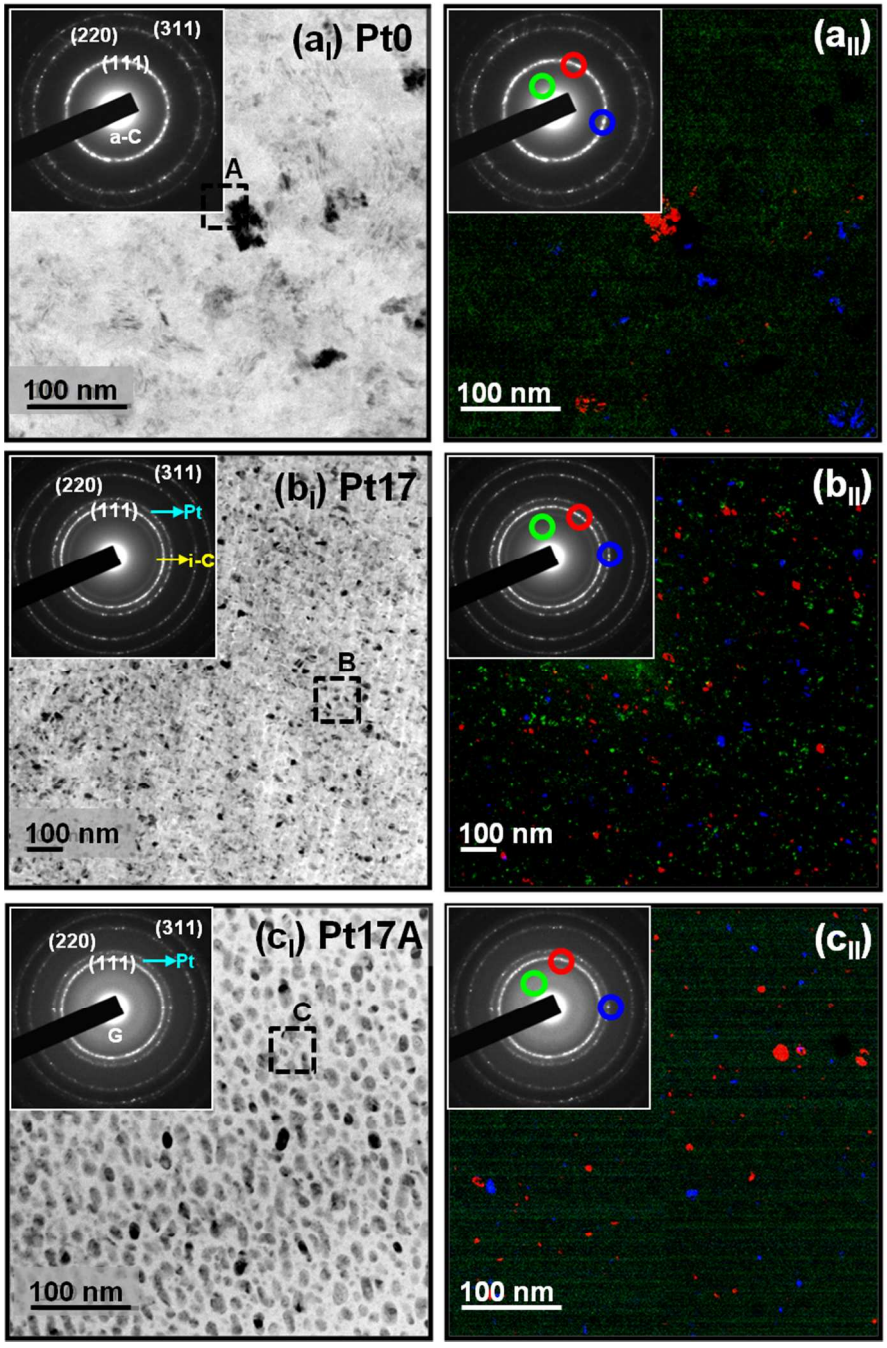

Figure 7

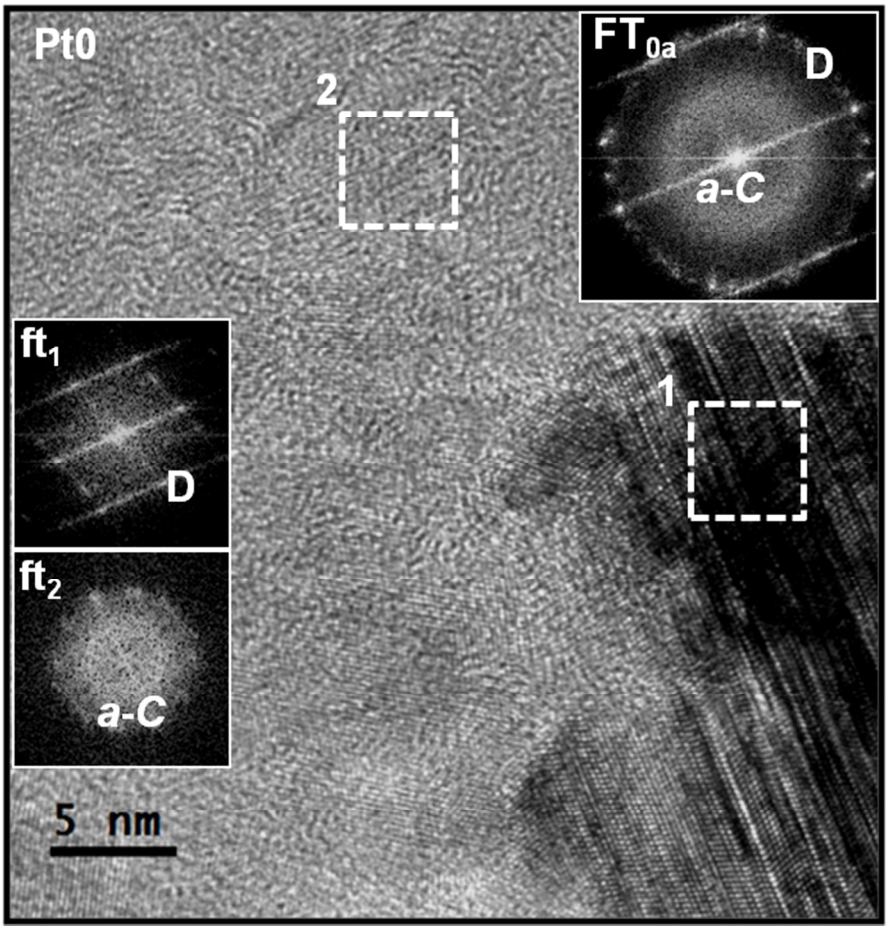

Figure 8

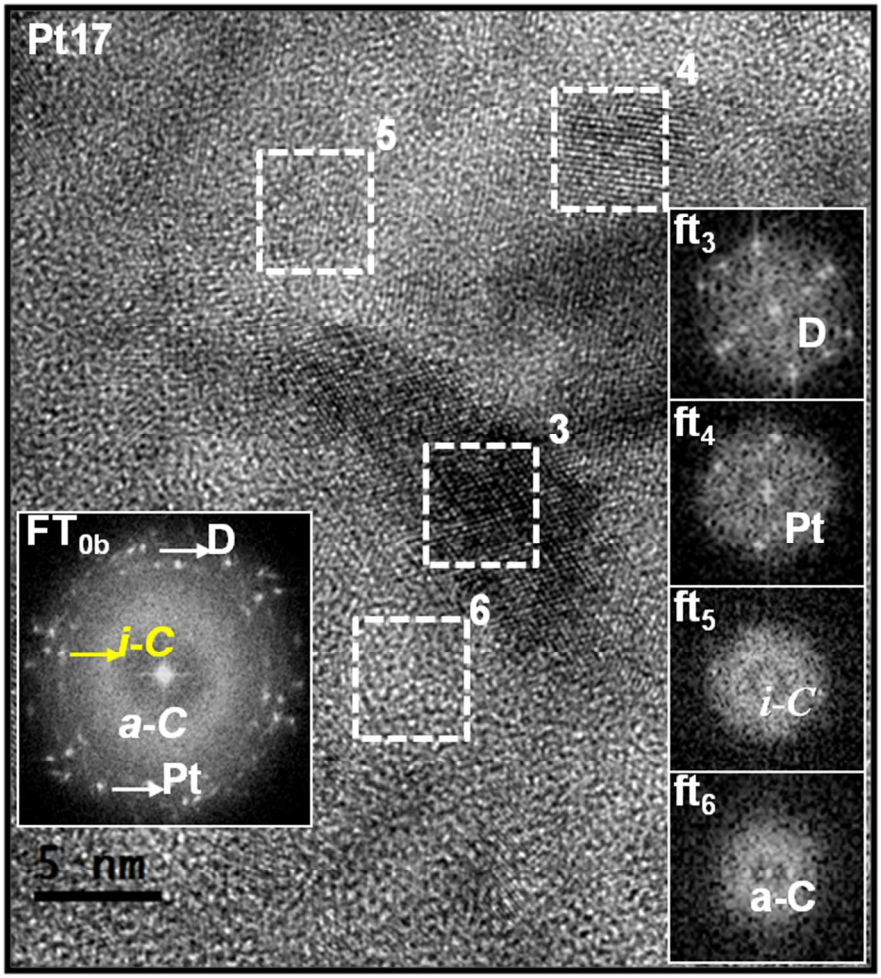

Figure 9

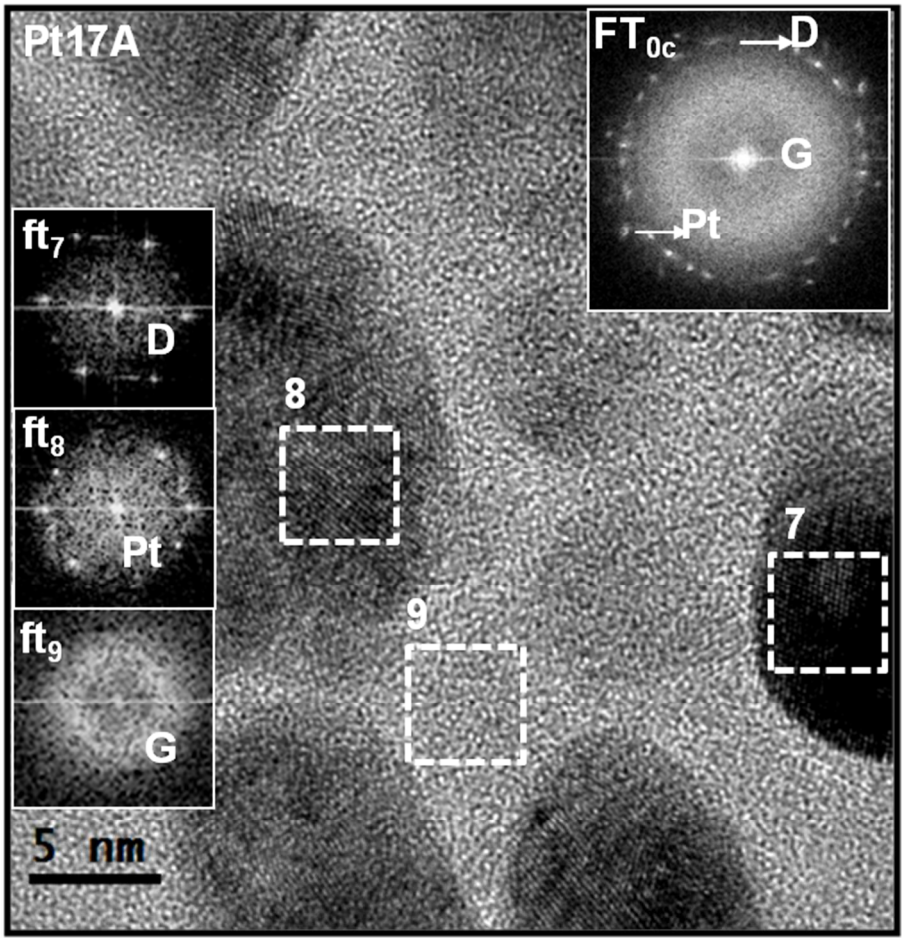

Figure 10

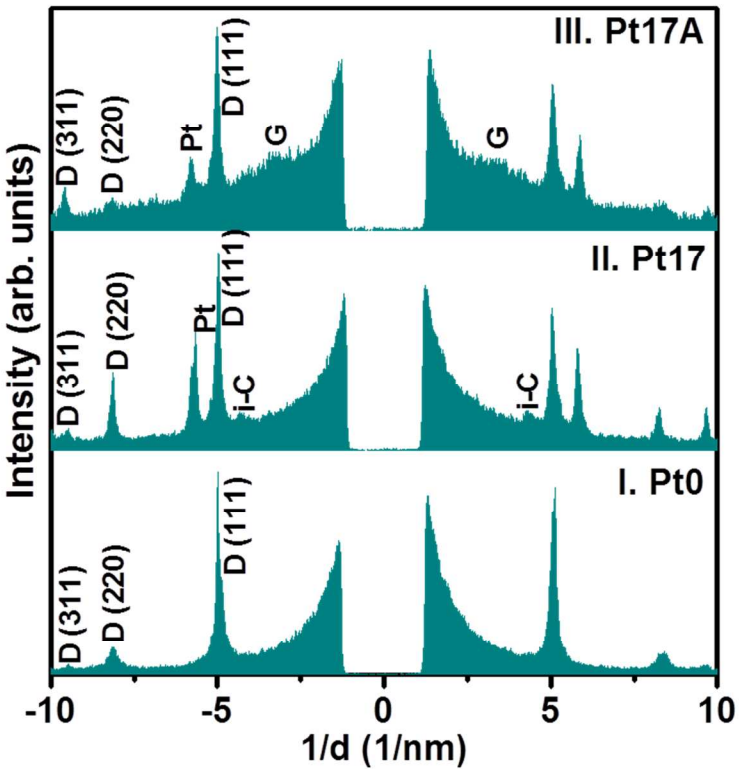

Figure 11

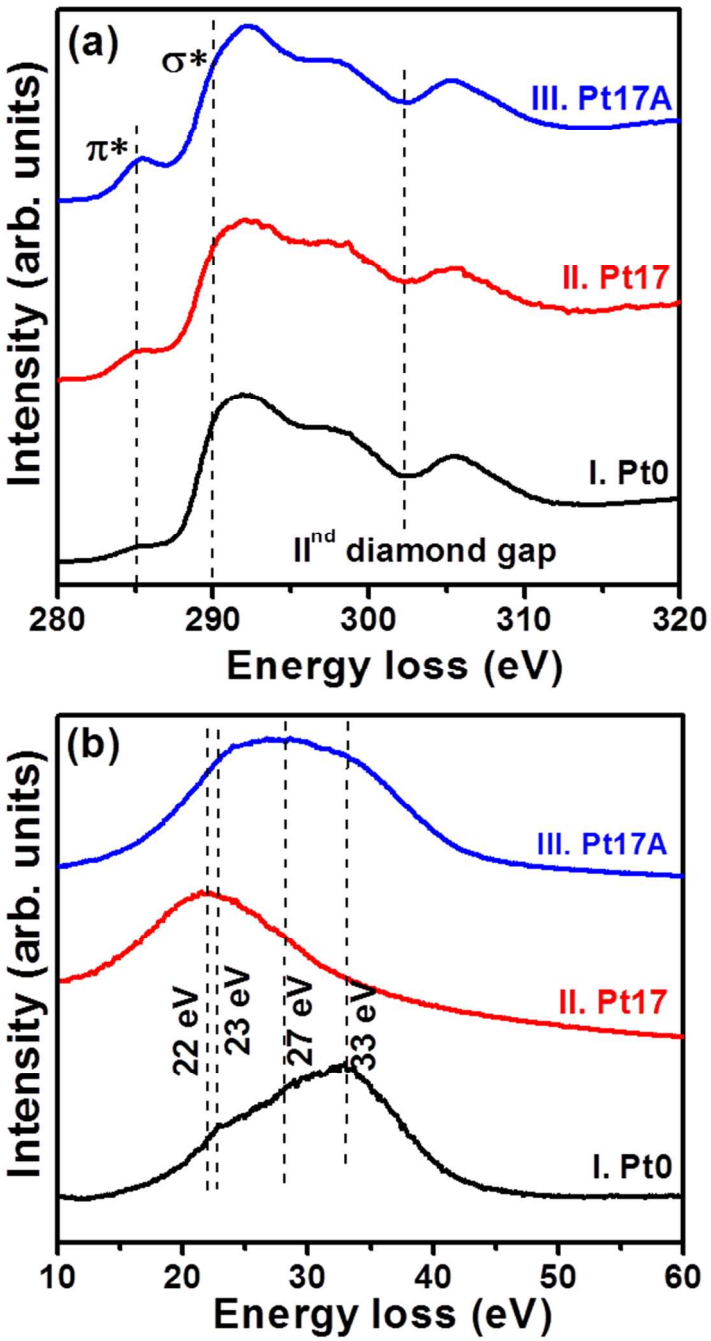

Figure 12

Table of contents:

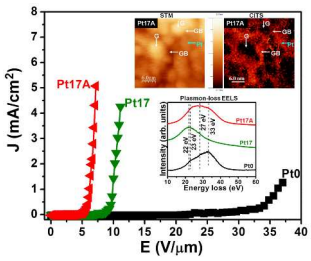

Pt nanoparticles catalytically induce nanographitic phases in grain boundaries achieving highly conducting ultrananocrystalline diamond films with enhanced EFE properties